



Pergamon

Acta Materialia 50 (2002) 4061–4073



www.actamat-journals.com

# Coarsening of ordered intermetallic precipitates with coherency stress

V. Vaithyanathan \*, L.Q. Chen

*Department of Materials Science and Engineering, The Pennsylvania State University, University Park, PA 16802, USA*

Received 20 November 2001; received in revised form 21 May 2002; accepted 23 May 2002

## Abstract

The morphological evolution and coarsening kinetics of ordered intermetallic precipitates with coherency stress were studied using a diffuse-interface phase-field model in two dimensions (2D). The emphasis is on the effects of precipitate volume fraction. The average aspect ratio of the precipitates in the microstructure is found to increase with time and decrease with volume fraction. Contrary to all the existing coarsening theories but consistent with a number of experimental measurements on the coarsening kinetics of ordered  $\gamma'$  precipitates in Ni-base superalloys, we found that the coarsening rate constant from the cubic growth law decreases as a function of volume fraction for small volume fractions ( $\leq 20\%$ ) and is constant for intermediate volume fractions (20–50%). From the simulation results, we infer that the two length scales in a stress-dominated coherent two-phase microstructure, the average precipitate size and average spacing between arrays of aligned precipitates, follow different growth exponents. It is demonstrated that as the volume fraction increases, the precipitate size distributions become broader and their skewness become increasingly positive. © 2002 Published by Elsevier Science Ltd on behalf of Acta Materialia Inc.

*Keywords:* Phase-field; Coarsening; Ni–Al; Coherent precipitates; Effect of volume fraction

## 1. Introduction

One of the most efficient ways to strengthen alloys is by introducing coherent precipitates through a controlled heat treatment process. This process, used commonly in metallic alloys, is referred to as the age hardening or aging or precipitation strengthening. The degree of strengthening depends on the volume fraction, size, morphology and spatial distribution of the second-phase pre-

cipitates. At high temperatures, the coherent precipitates undergo coarsening driven by a reduction in the total interfacial and elastic energy, resulting in an increase in their average size and an eventual loss of coherency, and thus causing a degradation of the mechanical properties of the alloy. Coarsening under the influence of coherency stress (stress arising from the difference in lattice parameters across the coherent interface) is significantly more complicated than the stress-free coarsening. First, the equilibrium compositions of the coherent two-phase mixture are usually different from those determined by the incoherent phase diagrams [1]. Secondly, the elastic properties are usually aniso-

\* Corresponding author. Fax: +1 814 234 8869.

E-mail address: vxv115@psu.edu (V. Vaithyanathan).

tropic, and hence result in nonspherical precipitate shapes [2–8]. In the extreme case, some overgrown precipitates may undergo splitting during aging [9–12]. Furthermore, the elastic interactions are infinitely long-range, which cause strong spatial correlations between the precipitates leading to their alignment along certain crystallographic directions [13–19]. Therefore, there are two distinct length scales in a coherent two-phase microstructure, the average precipitate size and average spacing between the arrays of aligned precipitates. Finally, the coarsening of ordered intermetallic precipitates is further complicated by the fact that they can exist in several types of antiphase domains related by a lattice translation to the parent disordered phase, and hence can either coalesce or remain separated by a disordered matrix layer depending on the antiphase relations of the neighboring domains.

As a result of the nonspherical precipitate shapes and strong spatial alignment of the coherent precipitates, there is ambiguity even in defining the precipitate size. It is not surprising that the experimental measurements on the coarsening kinetics of precipitates in the presence of coherency stress have produced conflicting results with some obeying the conventional  $t^{1/3}$  growth law for the average precipitate size, while others do not [20–23]. Experimental results on the dependence of coarsening kinetics on the precipitate volume fraction, in the presence of coherency stress, display a very different behavior compared to the stress-free coarsening. For example, Ardell et al [24,25] observed a surprising result: the coarsening rate constant decreases with increase in volume fraction for small volume fractions of  $\gamma'$  precipitates in Ni-base alloys. Since this behavior is contrary to all the existing coarsening theories [26–30] and experimental observations in stress-free systems, Ardell referred it as the “anomalous” coarsening behavior. Chellman and Ardell [31] found that the coarsening rate constant of  $\gamma'$  precipitates is independent of the precipitate volume fraction in the intermediate volume fraction regime ( $\sim 0.1$ – $0.6$ ), in Ni–Al binary alloys aged at 1073 K. On the other hand, Jayanth and Nash [32] showed that the coarsening rate constant increases with volume fraction for the same system at similar aging temperatures. This disagreement from the results of Jayanth and

Nash were attributed to the size measurements of precipitates with non-equiaxed and non-cuboidal shapes resulting from long aging times [33] and therefore cannot be compared with the coarsening results of Chellman and Ardell, which are from equiaxed precipitate shapes.

The purpose of this study is to investigate the morphological evolution and coarsening kinetics of coherent precipitates with significant lattice misfit and elastic anisotropy using the phase-field approach. In this paper, we discuss our two-dimensional coarsening results using a model alloy system similar to the  $\gamma'$ -Ni<sub>3</sub>Al precipitates in Ni-base superalloys. The emphasis is on the effect of volume fraction on the precipitate morphology and coarsening rate constant.

## 2. Model

Phase-field model [34] has been extensively used for microstructure simulation studies because of its ability to model complicated microstructures without any a priori assumptions. Each phase or domain in a microstructure is characterized by a set of field variables (for example, composition(s) and/or order parameter(s)). The interfaces (or domain boundaries) are regions where these field variables vary continuously from one phase (or domain) to another. We consider a model two-phase system, in which the parent phase has the disordered face centered cubic (FCC) structure and the precipitate phase belongs to an ordered L<sub>1</sub><sub>2</sub> (four interpenetrating simple cubes) structure. A composition field is required to characterize the composition distribution in a two-phase microstructure. Based on the crystallographic relations between the disordered and ordered phases, we also require three order parameter fields to describe the ordering from FCC→L<sub>1</sub><sub>2</sub> [35,36]. The temporal evolution of the field variables is given by the Cahn–Hilliard and Allen–Cahn (or Ginzburg–Landau) equations [37],

$$\frac{\partial c(\mathbf{r},t)}{\partial t} = M\nabla^2 \frac{\delta F}{\delta c(\mathbf{r},t)} + \psi(\mathbf{r},t) \quad (1)$$

$$\frac{\partial \eta_i(\mathbf{r},t)}{\partial t} = -L \frac{\delta F}{\delta \eta_i(\mathbf{r},t)} + \zeta_i(\mathbf{r},t) ; \quad i = 1,2,3 \quad (2)$$

where  $c$  is the solute composition and  $\eta_i$ s represent the long-range order parameters, which vary spatially ( $\mathbf{r}$ ) and temporally ( $t$ ).  $F$  is the total free energy of the two-phase microstructure,  $M$  is the solute mobility and  $L$  is the interfacial kinetic parameter (both  $M$  and  $L$  are assumed to be constants).  $\psi$ , and  $\zeta_i$ s are the random uncorrelated noise terms.

The total free energy of the system consists of the incoherent bulk free energy, the interfacial energy (gradient terms), and the elastic energy or coherency strain energy ( $E_{el}$ ). Assuming an isotropic interfacial energy, the chemical energy [ $F_{ch}$ , (incoherent bulk free energy+interfacial energy)], in the diffuse-interface description can be written as

$$F_{ch} = \int_V \left( f(c, \eta_i) + \frac{\alpha}{2} (\nabla c)^2 + \sum_{i=1}^3 \frac{\beta_i}{2} (\nabla \eta_i)^2 \right) dV \quad (3)$$

The gradient energy coefficients,  $\alpha$  and  $\beta_i$ s, are assumed to be independent of the field variables. The incoherent bulk free energy density  $f(c, \eta_i)$  is given by a polynomial of the field variables. The form of this coarse-grained free energy polynomial is based on the symmetry requirements of the FCC→L1<sub>2</sub> transformation [35,36,38,39].

$$\begin{aligned} f(c, \eta_1, \eta_2, \eta_3) = & \frac{1}{2} A_1 (c - C_1)^2 \\ & + \frac{A_2}{6} (C_2 - c) (\eta_1^2 + \eta_2^2 + \eta_3^2) + \frac{A_3}{3} (\eta_1 \eta_2 \eta_3) \\ & + \frac{A_4}{24} (\eta_1^4 + \eta_2^4 + \eta_3^4) + \frac{A_5}{24} (\eta_1^2 \eta_2^2 + \eta_2^2 \eta_3^2 + \eta_1^2 \eta_3^2) \end{aligned} \quad (4)$$

where the coefficients  $A_i$ s are functions of temperature and  $C_1$ ,  $C_2$  are constants with values close to equilibrium compositions of the matrix and precipitates, respectively. The coefficients and constants were chosen such that the free energy curve provides a *qualitative description* of the thermodynamics of Ni-Ni<sub>3</sub>Al at ~1000 K, with the constraint that  $A_3$  is non-zero for the order-disorder transformation to be first order. The free energy curve as a function of composition for the ordered phase, shown in Fig. 1, is obtained by minimizing Eq. (4) with respect to the order parameter (Fig.

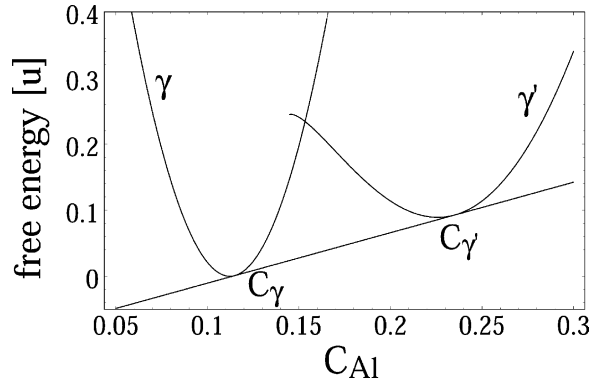


Fig. 1. Free energy curves of the disordered FCC ( $\gamma$ ) phase and the ordered L1<sub>2</sub> ( $\gamma'$ ) phase, expressed in units of [u]= $3.35 \times 10^7$  J/m<sup>3</sup> [42]. Common tangent construction provides the incoherent equilibrium compositions of the two phases.

1) (i.e. assuming the long-range order parameters are always at equilibrium for a given composition).

Khachaturyan's model [13] is used for the description of elastic energy arising from the lattice misfit, with a homogeneous modulus approximation. Assuming that the lattice parameter has a linear dependence on the solute composition (Vegard's law), the elastic energy functional can be written as

$$E_{el} = \frac{1}{2} \int_{\mathbf{k}} B[\mathbf{n}] |\tilde{c}(\mathbf{k})|^2 \frac{d^3 \mathbf{k}}{(2\pi)^3} \quad (5)$$

where the integral is over the reciprocal or Fourier space,  $\mathbf{n}$  ( $= \mathbf{k}/|\mathbf{k}|$ ) is a unit vector in the  $\mathbf{k}$  direction and  $\tilde{c}(\mathbf{k})$  is the Fourier transform of composition field  $c(\mathbf{r})$ . The function  $B(\mathbf{n})$  has all the information on the elastic properties of the system. It can be approximated in 2D [40] as

$$B(\mathbf{n}) \approx B_{el} \mathbf{n}_x^2 \mathbf{n}_y^2 \varepsilon_0^2 \quad (6)$$

$$B_{el} = - \frac{4(C_{11} + 2C_{12})^2}{C_{11}(C_{11} + C_{12} + 2C_{44})} \Delta \quad (7)$$

where  $C_{11}$ ,  $C_{12}$  and  $C_{44}$  are the independent coefficients in the elastic constant matrix,  $\Delta (= C_{11} - C_{12} - 2C_{44})$  is the elastic anisotropy factor and  $\varepsilon_0 [= (da/a)(1/dc)]$  is the coefficient of lattice expansion caused by the changes in composition.  $B_{el}$  is a material constant and positive in our case, since

the system is chosen to have a negative elastic anisotropy, similar to Ni-base superalloys.

### 3. Results

Simulations were performed by numerically solving the four nonlinear equations [Eqs. (1) and (2)], one for each field variable, using the semi-implicit Fourier-Spectral method [41]). The coefficients of the free energy polynomial in Eq. (4) are obtained by a qualitative fit to the Ni-Ni<sub>3</sub>Al part of phase diagram at 1000 K along with the constraint that the equilibrium order parameter of  $\gamma'$  is  $\pm 1$ . The coefficients  $A_1$ ,  $A_2$ ,  $A_3$ ,  $A_4$  and  $A_5$ , expressed in units of  $3.35 \times 10^7$  J/m<sup>3</sup> [42], are 277.78, 66.67,  $-21.21$ , 22.14 and 22.14, respectively [since  $A_3$  is negative, the four translational domains of  $\gamma'$  are defined by  $(\eta_1, \eta_2, \eta_3) = (1, 1, 1)$ ,  $(-1, -1, 1)$ ,  $(-1, 1, -1)$  and  $(1, -1, -1)$ ]. The constants  $C_1$  and  $C_2$  in the free energy polynomial are 0.1123 and 0.2211, respectively. These values have been chosen to produce a driving force for decomposition from a disordered FCC single-phase to a two-phase mixture of ordered and disordered phases similar to that obtained in the CALPHAD database for Ni-alloys. The gradient energy coefficient  $\beta$  (assuming  $\alpha$  to be zero) is chosen to be  $4 \times 10^{-11}$  J/m, which gives rise to an interfacial energy of  $\sim 25$  mJ/m<sup>2</sup> based on Cahn's theory [43]. The assumption that the concentration gradient coefficient ( $\alpha$ ) is zero is a simplification which does not affect the main results on the volume fraction dependence of coarsening rate constants. The interfacial energy value of 25 mJ/m<sup>2</sup> used in the simulation is reasonable, because the experimentally estimated values show a wide range from 8 mJ/m<sup>2</sup>–80 mJ/m<sup>2</sup>. The coefficient  $B_{el}$  in the elastic energy equation [Eq. (7)] is estimated as  $120 \times 10^{10}$  J/m<sup>3</sup>, based on the elastic constants of Ni solid solution ( $C_{11} = 209$  GPa,  $C_{12} = 149$  GPa and  $C_{44} = 96$  GPa at 1000 K) from the work of Prikhodko et al [44]. The misfit strain used in the simulation is  $\sim 1\%$ , similar in magnitude to the strain values observed in Ni-base superalloys (Ni-Ni<sub>3</sub>Al  $\sim 0.5\%$  and Ni-Ni<sub>3</sub>Ti  $\sim 1\%$ ). With these parameters, the interface width was estimated as  $\sim 3.5$  nm, comparable to the diffuse-interface width estimated from

cluster variation method for Al-Al<sub>3</sub>Li interface [45].

The size of the simulation cell used in this study is  $\sim 1.3$ – $1.9$   $\mu\text{m}^2$  depending on the precipitate volume fraction. It should be emphasized that the biggest difficulty associated with studying coarsening using computer simulations is the need for large systems, which can accommodate a few thousand precipitates to ensure good statistics. This enforces a severe restriction on studying small volume fractions ( $\leq 10\%$ ), as the computational time and memory required for the simulation scales with system size. All the coarsening simulations reported here begin with a few thousand precipitates in the initial stages and were allowed to coarsen to a few hundred precipitates.

$\Delta x$  (or the grid spacing) is chosen such that the interface contains enough grid points to remove the artifacts from the underlying discretizing lattice.  $\Delta t$  (or the time step) is chosen to ensure a stable solution. Six precipitate volume fractions, 0.1, 0.2, 0.35, 0.5, 0.7 and 0.9, were studied with the same kinetic parameters to determine the effect of volume fraction on the morphology and coarsening kinetics. In all cases, the initial configuration is a disordered supersaturated solid solution. Since our focus is only on the coarsening kinetics and not the sequence of transformation, this assumption does not affect our results. The noise terms aid the nucleation by overcoming the nucleation barrier and are removed after nucleation. The precipitate microstructure and coarsening kinetics are then extracted from the simulation results, which are averaged over two simulation runs with different but statistically similar initial conditions.

#### 3.1. Morphology evolution

Fig. 2 shows the morphology evolution of model  $\gamma'$  precipitates for 20% precipitate volume fraction. The coherent precipitates are shown in white in a dark matrix. We observe the anisotropic elastic energy induced cuboidal shape change of precipitates and the anisotropic elastic interaction induced alignment along elastically soft [10] or [01] directions, known from previous experiments and simulations. The aspect ratio of precipitates were calculated to quantify the morphological

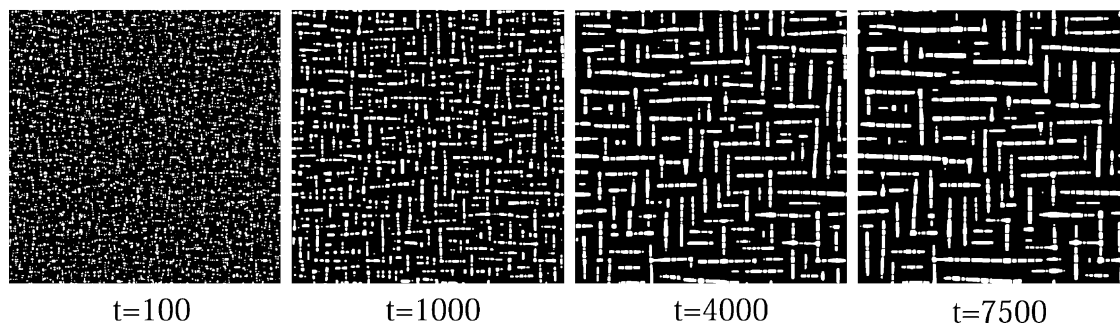


Fig. 2. Microstructure evolution of the model  $\gamma'$  precipitates for 20% precipitate volume fraction. With  $\sim 3500$  precipitates after nucleation ( $t=100$ ), precipitate coarsening was followed until the late stages ( $t=7500$ ) with  $\sim 400$  precipitates remaining. All time values expressed in the results are dimensionless time.

evolution. Following Qiu [22], the fraction of precipitates with different aspect ratios (volume of precipitates with different aspect ratios, normalized by the total precipitate volume in the microstructure) is expressed as a function of time. Such a morphology evolution plot for 20% equilibrium precipitate volume fraction is shown in Fig. 3. The precipitate shapes are represented by different aspect ratio ( $AR$ ):  $AR=1$  ( $AR < 1.5$ ) implies precipitates with circular or square shapes,  $AR=2$  ( $1.5 < AR < 2.5$ ) represents rectangular-shaped precipitates, and  $AR=3$  ( $2.5 < AR < 3.5$ ) and 4

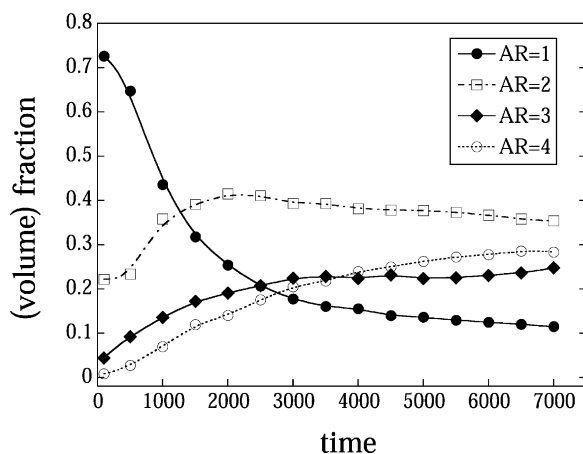


Fig. 3. Morphology evolution plot showing the fraction of precipitates with different aspect ratios as a function of time for 20% precipitate volume fraction ( $AR$ -aspect ratio). It exhibits excellent qualitative agreement with the experimental result of Qiu [22], based on SEM observations of  $\gamma'$  precipitates in Ni-Al alloys.

( $AR > 3.5$ ) represent plate-shaped precipitates. From the morphology evolution plot, it is clear that the fraction of precipitates with square shape decreases with time and the fraction of precipitates with larger aspect ratios increases with time, resulting in an overall increase in the average aspect ratio of precipitates with time. The simulated morphology evolution plot (Fig. 3) shows excellent qualitative agreement with the experimental result of Qiu [22], based on scanning electron microscopy (SEM) measurements from Ni-Al alloy.

The precipitate morphology dependence on their volume fraction is shown in Fig. 4, with individual microstructures from six different volume fractions from the late stages of coarsening. The most notable feature from the microstructures is the breakdown of precipitate array structure at large volume fractions ( $> 50\%$ ). Fig. 5 provides a quantitative comparison of the precipitate morphology from the late stages of coarsening as a function of their volume fraction. This morphology characterization plot (calculated similar to Fig. 3) is a quantitative substitute for the precipitate morphologies shown in Fig. 4. As the precipitate volume fraction increases, the fraction of plate-shaped precipitates decreases and the fraction of square-shaped (equiaxed) precipitates increases dramatically. The presence of four types of antiphase domains with unstable antiphase domain boundaries and the spatial constraints to growth at large precipitate volume fractions can explain this observation. Fraction of rectangular precipitates ( $AR=2$ )

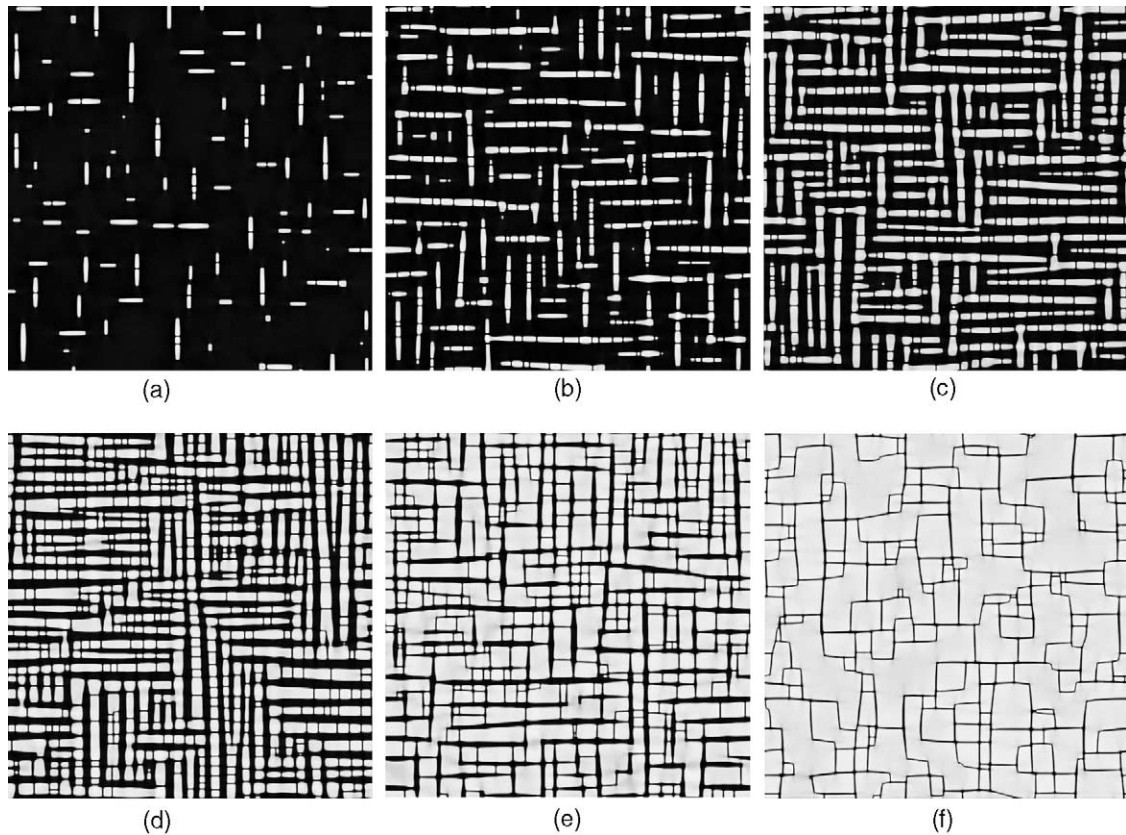


Fig. 4. Morphology of  $\gamma'$  precipitates from the late stages of coarsening are compared for six precipitate volume fractions. (a) 0.1, (b) 0.2, (c) 0.35, (d) 0.5, (e) 0.7 and (f) 0.9.

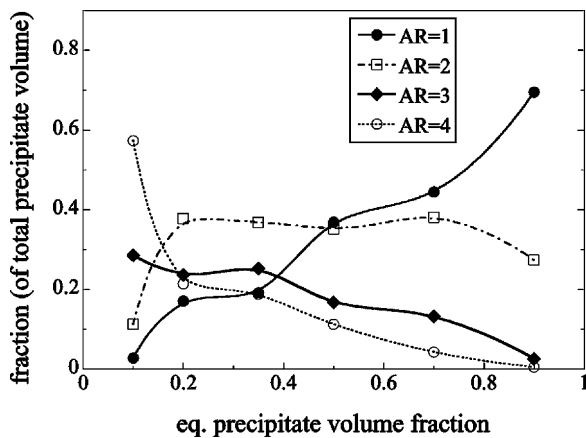


Fig. 5. Fraction of precipitates with different aspect ratios as a function of the equilibrium precipitate volume fraction from the microstructures shown in Fig. 4 (AR=aspect ratio).

remains fairly constant in the intermediate volume fraction range. These morphological features of  $\gamma'$  precipitates as a function of volume fraction observed from the simulation results, were also evident from the dark-field micrographs of Chellman and Ardell [31].

The volume fraction dependence of precipitate morphology can also be compared using the precipitate size distributions. The scaled precipitate size distribution, also referred to as the discrete probability density function, is constructed from the probability of occurrence of precipitates in small discrete intervals of normalized radius (radius normalized by average radius). Since the precipitate size distributions exhibit a good scaling behavior, they are represented by an averaged precipitate size distribution for each volume fraction (in Fig. 6), the average performed over data col-

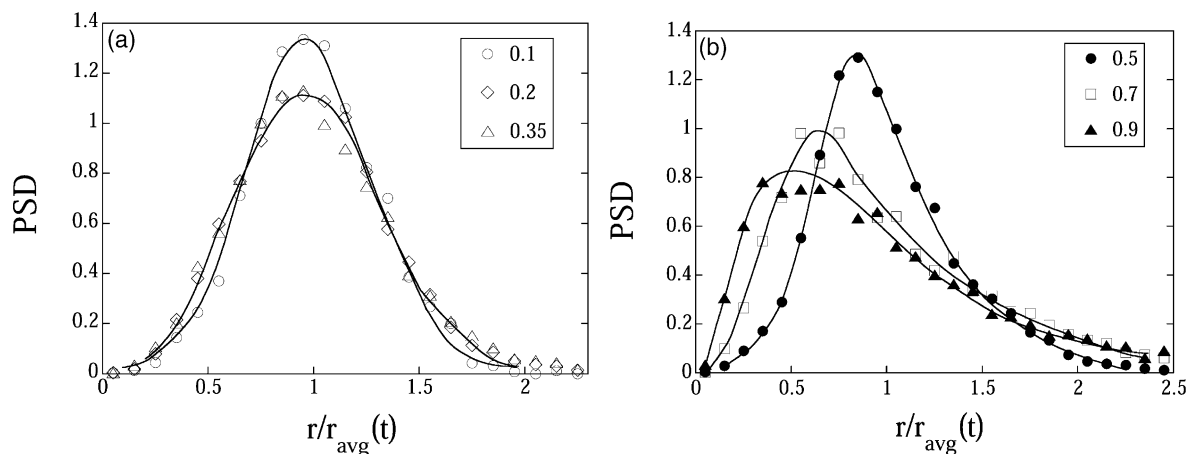


Fig. 6. Comparison of scaled precipitate size distributions averaged from the late stages of coarsening for six precipitate volume fractions (the guiding curves for the distribution are just hand drawn).

lected from the late stages. The position of maximum and breadth of the distribution remains fairly constant for the small and intermediate volume fractions ( $\leq 50\%$ ). For large volume fractions, increase in volume fraction shifts the position of maximum to smaller normalized precipitate size and also results in an increase in the breadth of the distribution. The statistics obtained from the precipitate size distributions as a function of volume fraction are shown in Table 1. The standard deviation is a measure of the breadth of the curve, the skewness provides a measure of its shape and kurtosis is a measure of its deviation from a normal distribution. The breadth of the distribution increases with precipitate volume fraction (though the variation is small for intermediate volume fractions), a result also unique to all the conven-

tional coarsening theories [26–30]. Skewness becomes more positive with increase in volume fraction, while kurtosis values exhibit no volume fraction dependence (arbitrary). The precipitate size distributions for the six different volume fractions were very different from the 2D-LSW (Lifshitz, Slyozov and Wagner) distribution [46–48], which represents the distribution in the zero volume fraction limit.

### 3.2. Growth law

The most commonly investigated aspect of coarsening kinetics is the Ostwald Ripening or growth law, which is a power law expressing the average length scale evolution as a function of time.

Table 1

Statistical parameters from the scaled and averaged precipitate size distributions for the six volume fractions shown in Fig. 6. Statistics for the 2D-LSW distribution was obtained based on the distribution from Rogers and Desai [48]

Equilibrium volume fraction	Standard deviation	Coefficient of skewness	Coefficient of kurtosis
0.10	0.302	0.176	0.044
0.20	0.358	0.462	0.430
0.35	0.374	0.497	0.304
0.50	0.378	0.776	0.828
0.70	0.537	0.930	0.477
0.90	0.599	0.983	0.571
LSW (2D, $\phi \rightarrow 0$ )	0.2	-1.085	1.132

$$R_{\text{avg}}(t)^n = R_0^n + K t \quad (8)$$

where  $R_{\text{avg}}(t)$  is the time-dependent average precipitate size or length scale,  $R_0$  is the average precipitate size or length scale at the start of coarsening,  $K$  is the coarsening rate constant, which is a function of the equilibrium precipitate volume fraction, and  $n$  is the growth law or coarsening exponent. Conventional theories showed that the exponent,  $n$ , is 3 for diffusion-controlled coarsening and 2 for interface reaction-controlled coarsening, in the absence of coherency stress. For the particular case of  $\gamma'$  precipitates, because of their nonspherical shapes, a few different length scale measures are used to follow the temporal microstructure evolution. Most commonly used direct measures of the precipitate size are the half-edge length of cuboids, and the equivalent radius of a precipitate with same area. The inverse of first moment of the (circularly averaged) structure function [49] or its real-space analog [18,50] is also used as an indirect measure of the microstructure length scale. We examined all three of these length scale measures, namely, half-edge length, equivalent radius and inverse of first moment. The time-dependent length scales obtained from the simulation are used to extract the exponent and rate constant for each measure, based on a nonlinear least squares fitting of the growth law [Eq. (8)] and the results are shown in Table 2. The half-edge length and equivalent radius measures exhibit similar trend in the exponents and coarsening rate constants, but the inverse of first moment shows a

markedly different behavior (possible reasons will be discussed later). Although there is a high degree of uncertainty in the growth exponent in the presence of coherency stress, both the half-edge length and equivalent radius measures from this simulation study yield exponent values close to 3 for all the precipitate volume fractions. Based on a recent work by Thornton et al [51] and to be consistent with the analysis of experimental data [24,25,31,32], the growth exponent is fixed as 3 for examining the dependence of coarsening rate constant on precipitate volume fraction. Coarsening rate constant is the slope of the linear fit to cube of average size measure vs time (fit is restricted only to the linear portion of the data). The cube of half-edge length and inverse of first moment as a function of time and volume fraction are shown in Figs. 7 and 9, respectively.

The rate constant as a function of precipitate volume fraction obtained from the half-edge length measure (see Fig. 7) is displayed in Fig. 8. The rate constant exhibits an anomalous dependence on the precipitate volume fraction for small volume fractions (i.e., it decreases with volume fraction, contrary to the expected increase), remains nearly constant for intermediate volume fractions and increases with precipitate volume fraction for large volume fractions. A similar anomalous behavior for small volume fractions ( $\leq 10$ –15%) was observed by Ardell and coworkers [24,25] during the growth and coarsening of  $\gamma'$  precipitates in Ni-X (X-Al,Ti) alloys. The constant (or volume frac-

Table 2

Coarsening rate constant and the growth law exponent obtained from a nonlinear fit of the growth law, for six precipitate volume fractions. The exponents and coarsening rate constant obtained from three different length scale measures (HE-half-edge length, ER-equivalent radius, and IFM-inverse of first moment) are compared

Equilibrium volume fraction	Exponent 'n'			Coarsening rate 'K'		
	HE	ER	IFM	HE	ER	IFM
0.1	3.0	3.4	4.4	0.49	0.78	1.76
0.2	3.2	3.3	4.3	0.38	0.38	0.71
0.35	3.5	4.0	4.2	1.24	3.86	0.28
0.5	3.0 <sup>a</sup>	3.0 <sup>a</sup>	4.2	0.34	2.19	0.17
0.7	2.9	2.8	4.3	0.76	0.56	0.31
0.9	2.9	3.0	4.7	3.85	5.42	0.12

<sup>a</sup> Uncertainty from fit is large

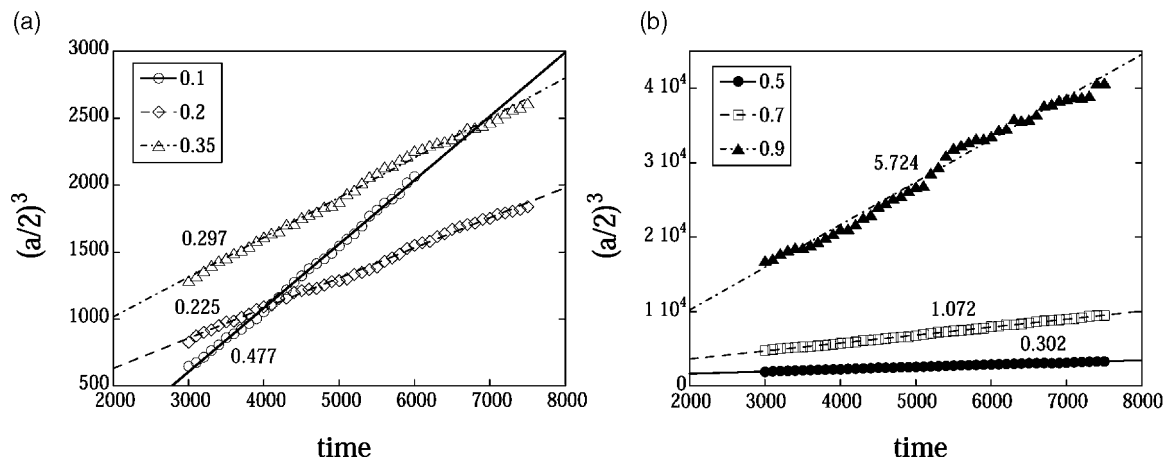


Fig. 7. Cube of half-edge length  $[(a/2)^3]$  vs time as a function of precipitate volume fraction. Slope of the linear fit (or the coarsening rate constant) is displayed next to the fit

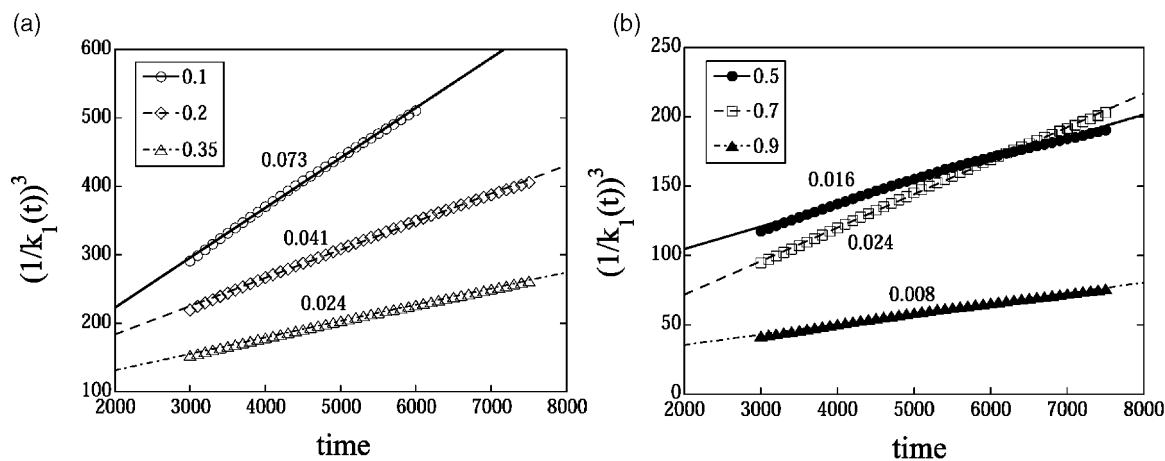


Fig. 9. Growth law behavior for the different precipitate volume fractions with inverse of first moment  $(1/k_1)^3$  as the length scale measure. Coarsening rate constant is extracted from the cube of inverse of first moment vs time. An exponent of 3.0 was used for easier comparison with the behavior in Fig. 7, though an exponent of 4.0 provided a more accurate fit.

tion independent) behavior of rate constants in the intermediate precipitate volume fraction range ( $\sim 20$ – $50\%$ ) from the simulation results is also in good agreement with the experimental observations of Chellman and Ardell [31] in Ni–Al alloy. This volume fraction independent behavior for intermediate volume fractions and anomalous behavior for small volume fractions were also observed in the case of low misfit  $\text{Ni}_3\text{Si}$  precipitates in Ni–Si alloy [52]. The rate constant dependence on precipitate volume fraction obtained from

the inverse of first moment measure displays no similarity with the direct real-space measures (half-edge length and equivalent radius); they instead exhibit a continuous decreasing trend as a function of precipitate volume fraction (see Fig. 9).

Since our focus was on the rate constant dependence on volume fraction, other dynamical aspects of the system are not discussed in detail. It has been verified that both the matrix composition and precipitate volume fraction are not constants during coarsening, but exhibit a linear behavior with

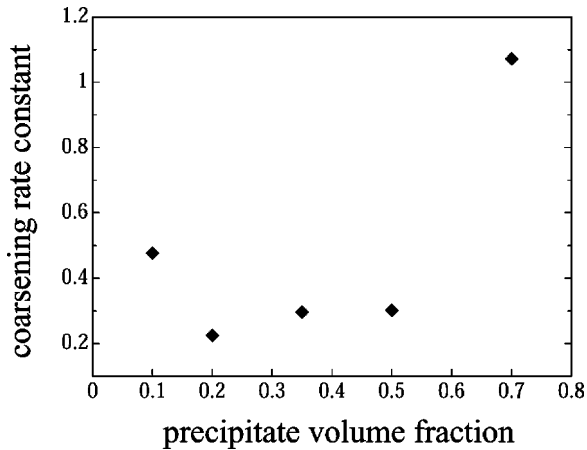


Fig. 8. Coarsening rate constant as a function of volume fraction obtained from the cube of half-edge length vs time (see Fig. 7). The rate constant for 90% volume fraction is not included because of the large scatter in the length scale data.

$t^{-1/3}$  in the late stages [53]. Initial results also reveal that the coherent equilibrium composition of the matrix (matrix composition as  $t \rightarrow \infty$ ) increases with the average composition of the alloy, in agreement with the results of Ardell and coworkers [31,54].

### 3.3. Discussion

The results from our 2D simulation study establishes the ability of phase-field model to realistically describe all the complexities involved in the coarsening of  $\gamma$  precipitates in Ni-alloys. For example, both the precipitates in our model system and  $\gamma$ -Ni<sub>3</sub>(Al,Ti) precipitates in Ni-alloys have four types of translational domains which strongly influence the coarsening process. The coalescence of any two of these domains will lead to the formation of an antiphase domain boundary (APDB), and is energetically favored only when the APDB energy is less than twice the interfacial energy. The model parameters are chosen such that the structural APDBs are unstable ( $\sigma_{\text{APDB}} > 2\sigma_{\text{int}}$ ), similar to Ni-base superalloys. It should be noted that the elastic inhomogeneity between the matrix and precipitates, even without the presence of antiphase domains, can give rise to similar microstructures; hard precipitates tend to be surrounded by soft matrix to minimize elastic energy [16,18,55]. How-

ever, experimental measurements in Ni-Al alloys indicate that the elastic inhomogeneity is small, leading to the conclusion that the aligned arrays of precipitates are a result of the combination of elastic interactions and the existence of antiphase relations among the precipitates in Ni-alloys.

The morphological evolution and its dependence on the volume fraction obtained from the simulation, including the aspect ratio and precipitate size distributions, show excellent qualitative agreement with the existing experimental observations in Ni-alloys. The precipitate morphology changes from cuboidal to complex faceted shapes with increase in volume fraction. The array structure of precipitates present for small and intermediate volume fractions ( $\leq 50\%$ ) breaks down for large volume fractions (see Fig. 4). This breakdown of array structure due to inter-array coalescence leads to complex faceted precipitate shapes for large volume fractions.

The *most interesting result*, however, is the prediction of decreasing coarsening rate constant with volume fraction for small volume fractions ( $< 20\%$ ). As far as we are aware, this is the first simulation result showing decreasing rate constant with volume fraction (anomalous behavior), although it has been experimentally observed in a number of Ni-base alloys [24,25,52]. In a prior simulation of the coarsening kinetics of  $\delta'$  (L1<sub>2</sub>-Al<sub>3</sub>Li) precipitates in an FCC matrix in Al-Li alloys [56] with a negligible lattice misfit ( $\sim 0.08\%$ ), the rate constant is found to increase with volume fraction throughout the entire volume fraction range. Since the crystallographic relations between the precipitates and matrix are the same in Ni-alloys and Al-Li alloys, the anomalous and constant coarsening rate constant behavior as a function of precipitate volume fraction in systems with lattice mismatch (Ni-alloys) must be due to the elastic interactions. Recent coarsening experiments on Ni-alloys revealed that the anomalous behavior extends to larger volume fractions as the lattice misfit increases [25]. The elastic interactions not only affect the rate constants, but also affect the shape of the precipitate size distributions. There is no change in the sign of skewness of size distributions with volume fraction for the model  $\gamma$  precipitates, as observed for the misfit-free  $\delta'$  precipi-

tates in Al-Li alloys both from the simulations and experiments [56,57]. The skewness of the  $\gamma$  precipitate size distributions from the simulation remains positive and increases with volume fraction in the entire volume fraction range.

It should be emphasized that the coarsening exponent in systems with strong elastic interactions remains to be controversial. Experimental results on Ni-Al alloys can be divided into two categories: one set of results claim that the coarsening exponent remains unchanged and change in kinetics due to coherency stress is reflected by the coarsening rate constant [24,31,32], while the other set of results show a change in kinetics reflected by a change in the coarsening exponent [22,23]. Based on numerical simulations, Leo et al [58] show that if scaling holds, the coarsening exponent in the stress dominated regime is 2. Nishimori and Onuki [16] have shown that the exponent in the late stages of coarsening is  $\sim 5$ . In this work, we use three different measures of length scale, namely, half-edge length, equivalent radius and inverse of first moment of structure function. Both the half-edge length and equivalent radius measures yield exponents close to 3.0 while the inverse of first moment yields exponents close to 4.0 (Table 2). While the half-edge length and equivalent radius measures correspond to the precipitate size, the inverse of first moment measure is related to the spacing between the arrays of precipitates rather than the precipitate size [13]. Coarsening of arrays of precipitates is quite different from conventional coarsening in which the precipitates are randomly distributed. Arrays of aligned precipitates disappear by a mechanism similar to the dislocation climb. Although further work is necessary to reach a firm conclusion, our results clearly indicate different growth exponents for the precipitate size (half-edge length and equivalent radius) measures and the spacing between the arrays of precipitates (inverse of first moment).

The growth exponent and coarsening rate constant dependence on volume fraction from the inverse of first moment measure are markedly different from the values and trend displayed by the real-space measures (see Table 2, Figs. 7 and 9). An exponent of 3 is used to obtain the coarsening rate constant from the inverse of first moment mea-

sure (in Fig. 9) to enable direct comparison with the growth law behavior from the half-edge length measure; an exponent of 4 provides a better fit and the rate constants display an identical volume fraction dependence as in Fig. 9. The inverse of first moment, as mentioned before, represents the inter-precipitate spacing in a general microstructure and in the case of Ni-alloys with aligned precipitates, it represents the spacing between the precipitate arrays. The decrease in coarsening rate constant from the array spacing as a function of volume fraction over the entire volume fraction range can be understood based on the following argument: the space constraints increasing with volume fraction lead to a reduction in the number of shrinking arrays by the climb-like mechanism, and results in precipitate growth within the array. This argument may not be extendable to large volume fractions ( $>50\%$ ) where the array structure of precipitates breaks down. It might be fortuitous that we observe a break in the decreasing rate constant trend on moving from 50 to 70% precipitate volume fraction (Fig. 9), where the array structure breaks down.

We would like to add a note of caution about the large volume fraction data. *The complex faceted precipitate shapes* caused by the breakdown of aligned array structures, due to excessive inter-array coalescence and the lack of experimental data for comparison at large volume fractions, increase the uncertainty in the quantitative nature of the rate constant and morphology evolution data for volume fractions  $>50\%$ . It is unclear if any of the available length scale measures are capable of capturing the coarsening of such complex shaped precipitates.

#### 4. Summary

The morphological evolution and coarsening kinetics of coherent precipitates in the presence of significant lattice mismatch is studied using a phase-field model. The emphasis is on the effects of precipitate volume fraction. It is shown that with increase in precipitate volume fraction, a larger fraction of precipitates have smaller aspect ratios due to space constraints and the presence of anti-

phase domains. The results are in excellent qualitative agreement with existing experimental measurements on Ni-base superalloys. Precipitate size distributions become broader and positively skewed with increase in volume fraction. The distributions are very different from the 2D-LSW prediction, and unlike all theoretical predictions, they exhibit positive skewness over the entire volume fraction range. Assuming a coarsening exponent of 3, the coarsening rate constant behavior from the average precipitate size measure as a function of volume fraction exhibits 3 distinct regimes: anomalous behavior (decreasing rate constant) for small volume fractions, no volume fraction dependence (constant) for intermediate volume fractions, and increasing rate constant with volume fraction for large volume fractions. Similar rate constant dependence on volume fraction has been experimentally observed for the  $\gamma'$  precipitates in Ni-base alloys.

### Acknowledgements

We would like to thank Dr. Zi-Kui Liu for providing free energy data from ThermoCalc for Ni-Ni<sub>3</sub>Al system. The authors are grateful for the financial support from the National Science Foundation under Grant DMR-01-22638. The computer simulations were performed on the Cray-T90 at the San Diego Supercomputer Center.

### References

- [1] Cahn JW. Acta Metall 1962;10:907.
- [2] Wang Y, Khachaturyan AG. Acta Metal. Mater 1995;43:1837.
- [3] Su CH, Voorhees PW. Acta Mater 1996;44:2001.
- [4] Leo PH, Lowengrub JS, Jou HJ. Acta Mater 1998;46:2113.
- [5] Johnson WC, Lee JK. Metall. Trans. A 1979;10:1141.
- [6] Abinandanan TA, Johnson WC. Acta Metall. Mater 1993;41:27.
- [7] Fratzl P, Penrose O, Lebowitz JL. J. Stat. Phy 1999;95:1429.
- [8] Lee JK. Scr. Metal Mater 1995;32:559.
- [9] Doi M, Miyazaki T, Wakatsuki T. Mater. Sc. Eng. 1985;74:139.
- [10] Khachaturyan AG, Semenovskaya SV, Morris Jr. JW. Acta Metall 1988;36:1563.
- [11] Doi M. Materials Transactions, JIM 1992;33:637.
- [12] Johnson WC, Voorhees PW. J. Appl. Phys. 1987;61:1610.
- [13] Khachaturyan AG. Theory of structural transformations in solids. NY: Wiley, 1983.
- [14] Ardell AJ, Nicholson RB. Acta Metall 1966;14:1295.
- [15] Sequeira AD, Calderon HA, Kostorz G. Scr. Metall. Mater 1994;30:7.
- [16] Nishimori H, Onuki A. Phys. Rev. B 1990;42:980.
- [17] Rubin G, Khachaturyan AG. Acta Mater 1999;47:1995.
- [18] Orlikowski D, Sagui C, Somoza A, Roland C. Phys. Rev. B 1999;59:8646.
- [19] Akaiwa N, Voorhees PW. Mater. Sc. Eng. 2000;A285:8.
- [20] Ardell AJ, Nicholson RB. J. Phys. Chem. Solids 1966;27:1793.
- [21] MacKay RA, Nathal MV. Acta Metall. Mater 1990;38:993.
- [22] Qiu YY. J. Mater Sc 1996;31:4311.
- [23] Doi M, Miyazaki T. In: Reichman S, editor. Superalloys. Warrendale: The Metall Soc; 1988. p. 66-3.
- [24] Maheshwari A, Meshkinpour M, Ardell AJ. In: Pande CS, Marsh SP, editors. Modelling of Coarsening and Grain Growth. TMS; 1993. p. 2-3.
- [25] Kim DM, Ardell AJ. Scr. Mater 2000;43:381.
- [26] Ardell AJ. Acta Metal 1972;20:61.
- [27] Davies CKL, Nash P, Stevens RN. Acta Metall 1980;28:179.
- [28] Brailsford AD, Wynblatt P. Acta Metal 1979;27:489.
- [29] Tsumaraya K, Miyata Y. Acta Metall 1983;31:437.
- [30] Voorhees PW, Glicksman ME. Acta Metall 1984;32:2013.
- [31] Chellman DJ, Ardell AJ. Acta Metall 1974;22:577.
- [32] Jayanth CS, Nash P. Mater. Sc. and Tech 1990;6:405.
- [33] Ardell AJ. Scr. Metall. Mater 1990;24:343.
- [34] Chen LQ, Wang Y. JOM 1996;48:13.
- [35] Braun RJ, Cahn JW, McFadden GB, Wheeler AA. Phil. Trans. R. Soc. Lond. A 1997;355:1787.
- [36] Lai ZW. Phys. Rev. B 1990;41:9239.
- [37] Elder K. Comp. in Phys 1993;7:27.
- [38] Wang Y, Banerjee D, Su CC, Khachaturyan AG. Acta Mater 1998;46:2983.
- [39] Li Y, Chen LQ. Scr. Mater 1997;37:1271.
- [40] Wang Y, Chen LQ, Khachaturyan AG. In: Kirchner HO, Kubin L, Pontikis V, editors. Computer Simulation in Materials Science. 1995. p. 32-5.
- [41] Chen LQ, Shen J. Comp. Phys. Comm 1998;108:147.
- [42] The free energy unit was fixed by comparison with the free energy calculated using ThermoCalc. Based on thermodynamics from ThermoCalc, the maximum driving force available for the FCC→L1<sub>2</sub> transformation in Ni-Ni<sub>3</sub>Al system at 1000 K is ~180 J/mole.
- [43] Cahn JW, Hilliard JE. J. Chem Phys 1958;28:258.
- [44] Prikhodko SV, Carnes JD, Isaak DG, Ardell AJ. Scr. Mater 1998;38:67.
- [45] Asta M. Acta Mater 1996;44:4131.
- [46] Lifshitz IM, Slyozov VV. J. Phys. Chem. Solids 1961;19:35.
- [47] Wagner C. Z. Elektrochem 1961;65:581.
- [48] Rogers TM, Desai RC. Phys. Rev. B 1989;39:11956.

- [49] Lebowitz JL, Marro J, Kalos MH. Acta Metall 1982;30:297.
- [50] Sequeira AD, Calderon HA, Kosterz G, Pedersen JS. Acta Metall. Mater 1995;43:3427.
- [51] Thornton K, Akaiwa N, Voorhees PW. Phys. Rev. Lett 2001;86:1259.
- [52] Cho JH, Ardell AJ. Acta Mater 1998;46:5907.
- [53] V. Vaithyanathan, *Phase-field simulations of coherent precipitate morphologies and coarsening kinetics*, PhD Thesis, Pennsylvania State University, (2002).
- [54] Ardell J, Maheshwari A. Acta Metall. Mater 1995;43:1825.
- [55] Hu SY, Chen LQ. Acta Mater 2001;49:1879.
- [56] Poduri R, Chen LQ. Acta Mater 1998;46:3915.
- [57] Mahalingam K, Gu BP, Liedl GL, Sanders TH. Acta Metall 1987;35:483.
- [58] Leo PH, Mullins WW, Sekerka RF, Vinals J. Acta Metall. Mater 1990;38:1573.